Electrical Oscillations in Microtubules

Md Mohsin[1], Horacio Cantiello[2], María del Rocío Cantero[2], and Marcelo Marucho[1,*]

[1]Department of Physics and Astronomy, University of Texas at San Antonio, San Antonio, Texas, USA.
[2]IMSaTeD, Instituto Multidisciplinario de Salud, Tecnología, y Desarrollo, CONICET-UNSE, Santiago del Estero, Argentina.
[*]Corresponding Author: marcelo.marucho@utsa.edu

ABSTRACT

Environmental perturbations and local changes in cellular electric potential can stimulate cytoskeletal filaments to transmit ionic currents along their surface. Advanced models and accurate experiments may provide a molecular understanding of these processes and reveal their role in cell electrical activities. This article introduces a multi-scale electrokinetic model incorporating atomistic protein details and biological environments to characterize electrical impulses along microtubules. We consider that condensed ionic layers on microtubule surfaces form two coupled asymmetric nonlinear electrical transmission lines. The model accounts for tubulin-tubulin interactions, dissipation, and a nanopore coupling between inner and outer surfaces, enabling luminal currents, energy transfer, amplification, and oscillatory dynamics that resemble the experimentally observed transistor properties of microtubules. The approach has been used to analyze how different electrolyte conditions and voltage stimuli affect electrical impulses' shape, attenuation, oscillation, and propagation velocity along microtubules. Integrating transistor-like properties in the microtubules model has profound implications for intracellular communication and bioelectronic applications.

Keywords: microtubule, electrical oscillation, leapfrogging, coupled nonlinear electrical transmission lines, intracellular information processing.

Introduction

Microtubules (MTs) are hollow cylindrical cytoskeleton polymers inside cells [1]. Apart from their well-known roles in controlling cell division, intracellular transport, and shape of the cells, MTs recently attracted attention for their polyelectrolyte properties. The significant number of the repeating units of ionic and ionizable groups make them highly negatively charged [2], acting like biological electrical wires with a high ionic conductivity approximately 15 times greater than the surrounding medium [3]. This MT's conductivity property has been measured in in-vitro experiments demonstrating that microtubules can transmit, amplify [4], and generate oscillating electrical signals [5, 6, 7] propagating axially along the microtubule and through their nanopores.

Substantial work has been done to provide a molecular understanding of these experimental data on MTs. According to Manning's theory [8, 9, 10], positive counterions condensate on their surface–a

characteristic shared with other biomolecular filaments like DNA and F-Actin–and move in response to applied electric fields in the form of ionic currents.

Pioneering approaches have modeled these biological electrical wires as single electrical transmission lines [11, 12, 13, 14], yielding non-perturbative Korteweg–de Vries (KdV) equations that predict ionic current propagating axially at near-uniform velocity. A more recent perturbative KdV model captured dissipation and damping contributions, predicting localized ionic wave packages (solitons) propagating with attenuated amplitudes and deceleration along actin filaments [15]. The approach also revealed that higher voltage inputs yield faster, narrower solitons, whereas lower inputs produce broader impulses. Meanwhile, intracellular environments exhibit lower electrical conductivity, higher capacitance, and broader double layers compared to the results obtained in in-vivo conditions. This multi-scale model also captured the impact of molecular conformational changes and solution protonation states, providing insights into pathological cytoskeletal conditions [16].

Single transmission line models for MTs [11, 12, 13, 14, 17, 18] have overlooked the ionic current through the lumen, electrical signal amplification, and oscillations. Although the lumen side of the MT has a lower surface charge compared to the outer and, therefore, less condensed ions, the asymmetric conduction of the nanopores [19] and the tail oscillation [20] can produce a notable luminal ionic current comparable to the outer one. This current can play a key role in the electrical energy transfer between the inner and outer surfaces, leading to self-sustaining and self-reinforcing oscillating coupled solitons traveling along each surface. This phenomenon already manifests in two coupled nonlinear transmission lines (NLTLs) characterizing electrical networks in other fields [21, 22]. In these systems, solitons along each transmission line form bound state pairs, known as leapfrogging solitons, propagate with opposite phases at nearly equal velocities, transfer electrical energy alternately from the leading soliton to the trailing soliton, giving rise to oscillations as they continuously overtake each other periodically.

Moreover, in a transistor model for MT oscillations, the concept of time-variant pore conductance aligns naturally with electrochemical gating, where the nanopores function as dynamic control elements, similar to the gate of a transistor. It can envision how this phenomenon can fit into different transistor analogies.

In a Bipolar Junction Transistor (BJT) analogy (originally postulated in [4]), the base current would control the much larger collector-emitter current. In MTs, the nanopores' conductance and small modulations in local ionic gating, such as protonation-deprotonation cycles or divalent cation binding, would lead to significant changes in transmembrane ionic flow, where the nonlinear gain observed in MTs resembles transistor-like amplification.

In a MOSFET, the gate voltage modulates the channel conductivity by controlling charge carrier density. In this case, the nanopores in the MT, acting as gates, could modulate ionic currents through local changes in charge distribution, possibly driven by binding/unbinding of ions or conformational shifts. In MTs, local ionic depletion or enrichment in the nanopores could control the current flow, acting as a dynamic gating mechanism, where cyclic shifts in depletion/enrichment regions, driven by feedback from

the intrinsic electrical activity, could help emerge the observed oscillations. A transistor with dynamic conductance would also behave similarly to a memristor, where the history of charge movement influences future conductance [23]. This hypothesis is supported by the hysteresis observed in the conductance due to ionic conditions. This suggests that MTs might retain state-dependent conductance, reinforcing the analogy with adaptive bioelectronic transistors (Cantiello, unpublished observations). Additionally, MTs exhibit voltage-dependent resonance frequencies, suggesting an intrinsic field-effect behavior where the conductance oscillates due to internal charge-wave interactions.

Thus, the time-variant conductance of nanopores in MTs fits well into a transistor-based framework, particularly one where ionic gating modulates electrical properties dynamically. This supports the core idea that MTs function as biological semiconductors, where oscillatory gating enables information processing and amplification.

Based on these premises, in this article, we introduce a novel approach that considers condensed ionic layers on the outer and inner surfaces of the MT to form a pair of coupled nonlinear electrical transmission lines generating leapfrogging solitons. Additionally, counterions are exchanged between the inner and outer transmission lines through nanopores characterized by a nonlinear voltage-dependent resistance that resembles the transistor properties of MTs. We used Kirchoff's law to solve these electric circuits, obtaining two coupled perturbative KdV equations, one for the outer and one for the inner NLTL. We applied an adiabatic perturbation theory to transform these two third-order coupled differential equations [24] into four coupled first-order differential equations, two for the soliton phases and two for their amplitudes. We solved these equations numerically using Mathematica software. We also derived simple, easy-to-evaluate approximate analytical solutions for practical applications. Illustrative images and more details on the approach and the solution are provided in the Methods section and supplementary document. The approach has been used to determine the effects of electrolyte conditions and voltage stimulus on the electrical impulse shape, attenuation, oscillation, and propagation velocity along MTs.

Results

In Fig. 1, we present the time evolution of the outer and inner (lumen) voltage signal solutions $V(x,t)$ and $W(x,t)$ for input voltages of 0.04V and 0.08V. The results display oscillatory traveling solitons at increasing (snapshot) distances $x = 0.1$, 2.6, 4.6, 6.6, 8.6, 10.6, 12.6, and 14.6 μm along the MT. The electrical double layer (EDL) on MT's outer and lumen surfaces was characterized using the asymmetric condensed ionic layer parameters provided in the Methods section.

The soliton dynamics along the MT were obtained using eq. 13 in ref. [15] and the model parameter values mentioned above. The results are presented in Fig. 2, showing opposite-in-phase oscillations between the outer and inner soliton propagation velocities.

Additionally, we determined the soliton oscillation frequency by analyzing the time-dependent signal defined by the difference $\kappa_1(\tau) - \kappa_2(\tau)$, derived from the numerical solutions of the model equations. The signal was sampled over a uniform grid in dimensionless time τ, and the local maxima were identified

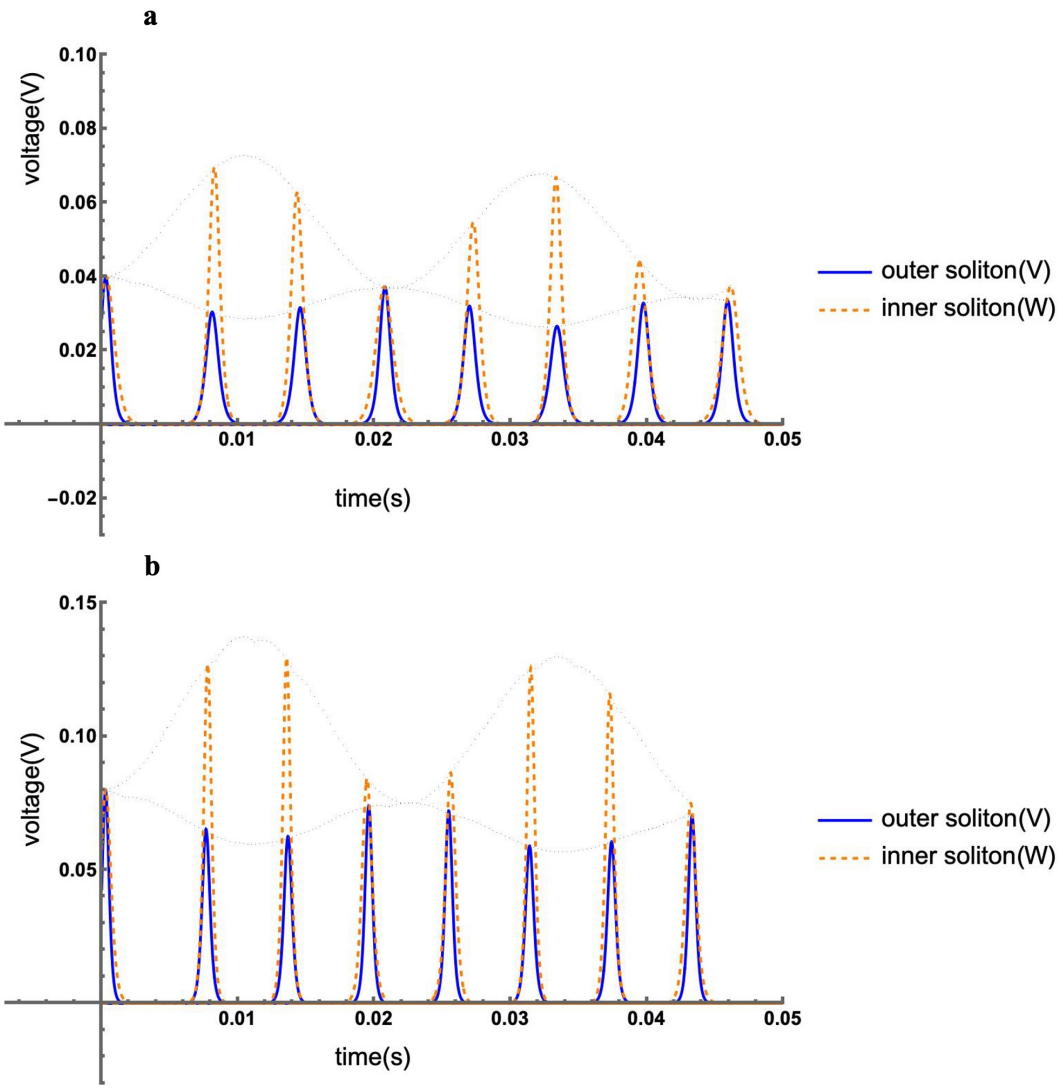

Figure 1. Soliton-like voltage propagation along the MT under asymmetric ionic conditions.Time evolution of the outer voltage $V(x,t)$ and inner (lumen) voltage $W(x,t)$ for input voltages of 0.04 V (a) and 0.08 V (b) at increasing positions along the microtubule: x = 0.1 , 2.6 , 4.6 , 6.6 , 8.6 , 10.6 , 12.6 , 14.6 μm. The black dotted line represents the soliton amplitude peak oscillation.

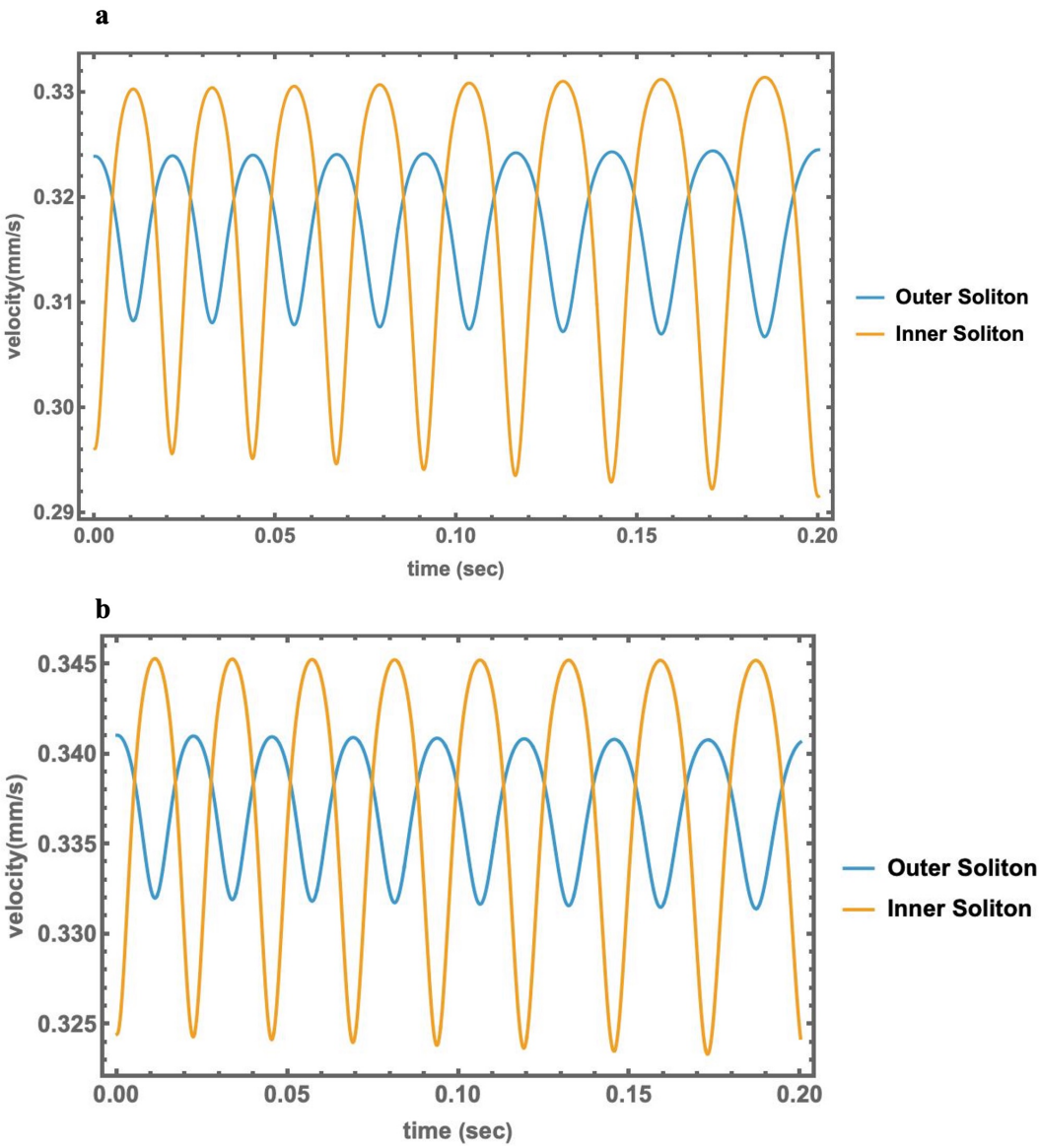

Figure 2. Soliton propagation velocities along the MT. (a) Input voltage 0.04 V. (b) Input voltage 0.08 V. These results correspond to the soliton-like voltage propagation described in Fig. 1.

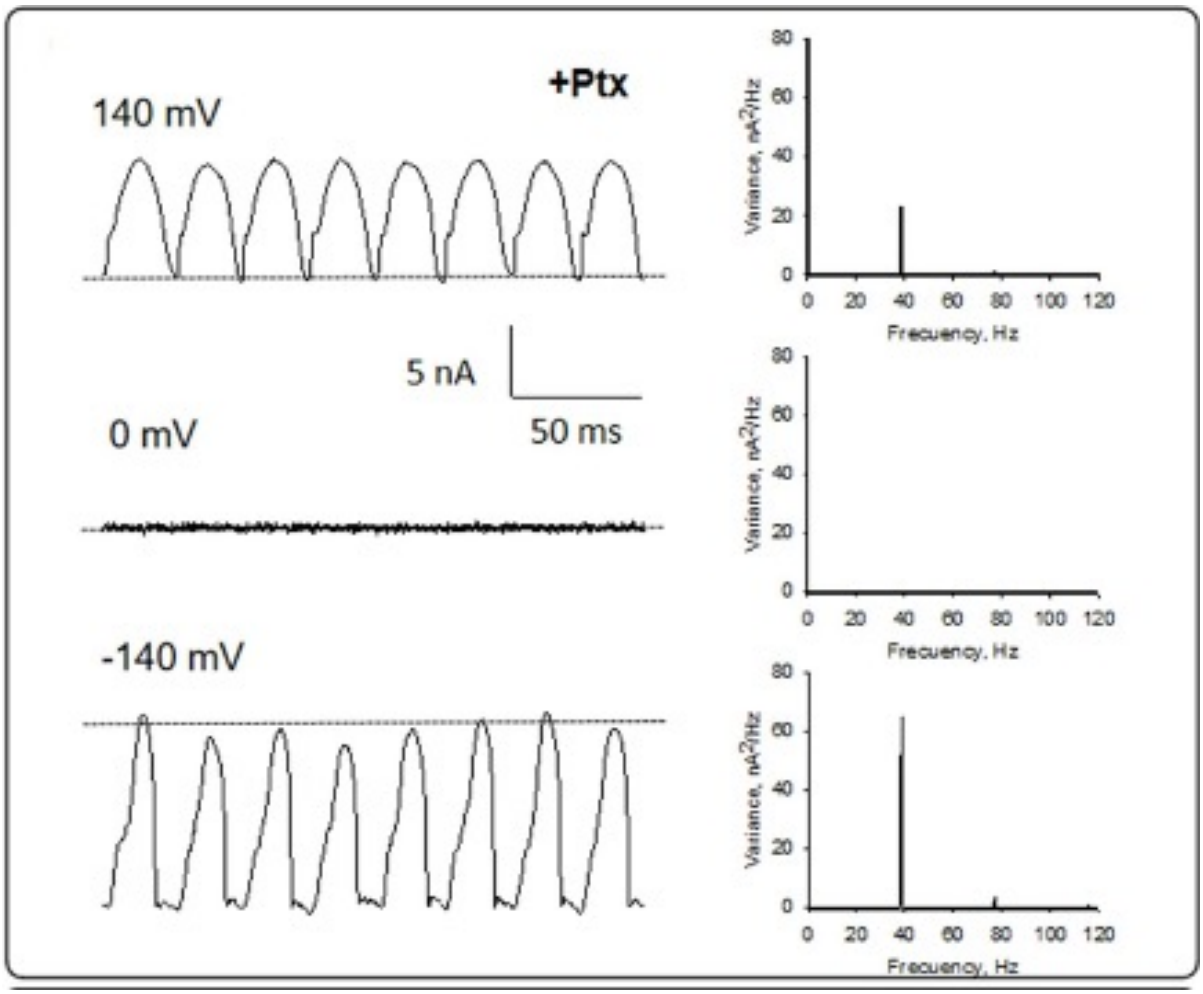

Figure 3. Experimental soliton oscillation frequencies. Current oscillations of Paclitaxel-stabilized isolated MTs. (Left) Current fluctuations at different holding potentials. (Right) Linear–linear plots of the Fourier power spectra obtained from tracings shown on the Left. The fundamental frequencies can be observed on the spectra (Ref. [7]).

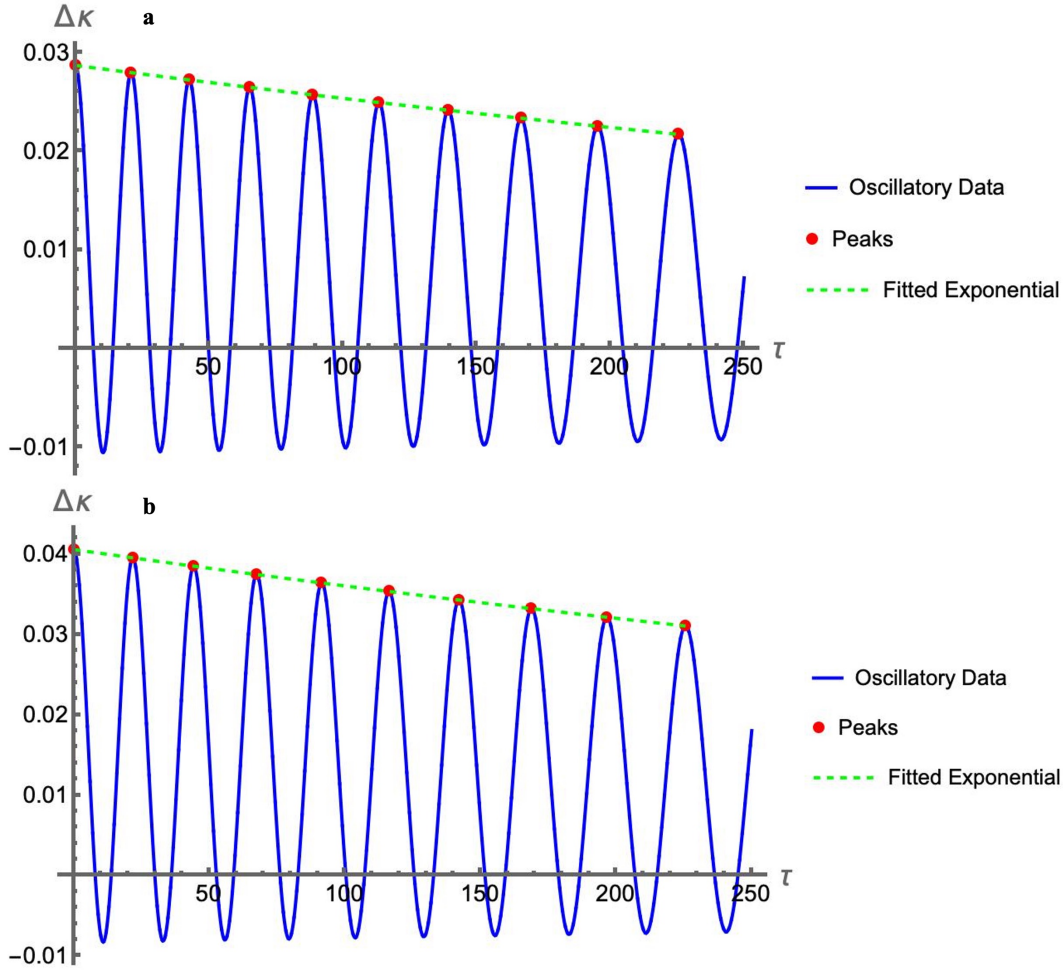

Figure 4. Soliton amplitude attenuation and damping parameter estimation. Exponential fitting of soliton peak amplitudes as a function of dimensionless time τ. (a) Input voltage 0.04 V. (b) Input voltage 0.08 V. Red points represent the soliton peak locations. These results correspond to the soliton-like voltage propagation described in Fig. 1.

using a peak detection algorithm. From the position of the successive peaks, we computed the mean oscillation period $\Delta\tau$, which was then converted to a physical frequency using the relation $t = (24\alpha)\tau$. This yielded a dominant frequency of approximately 39 Hz, consistent with measurements from voltage-clamp experiments (see Fig. 3).

The result shows reasonable agreement with the theoretical prediction obtained from the approximate analytical expression given in equation 18:

$$\omega_0^2 = \frac{8A}{15}\left(M_2 + M_4\right)\kappa^3$$

which corresponds to a frequency of 45.77 Hz. While the theoretical frequency overestimates by ~17% the numerically obtained value (39 Hz), the discrepency may be attributed to the approximations inherent in the analytical derivation and the nonlinearities captured in the full numerical solution.

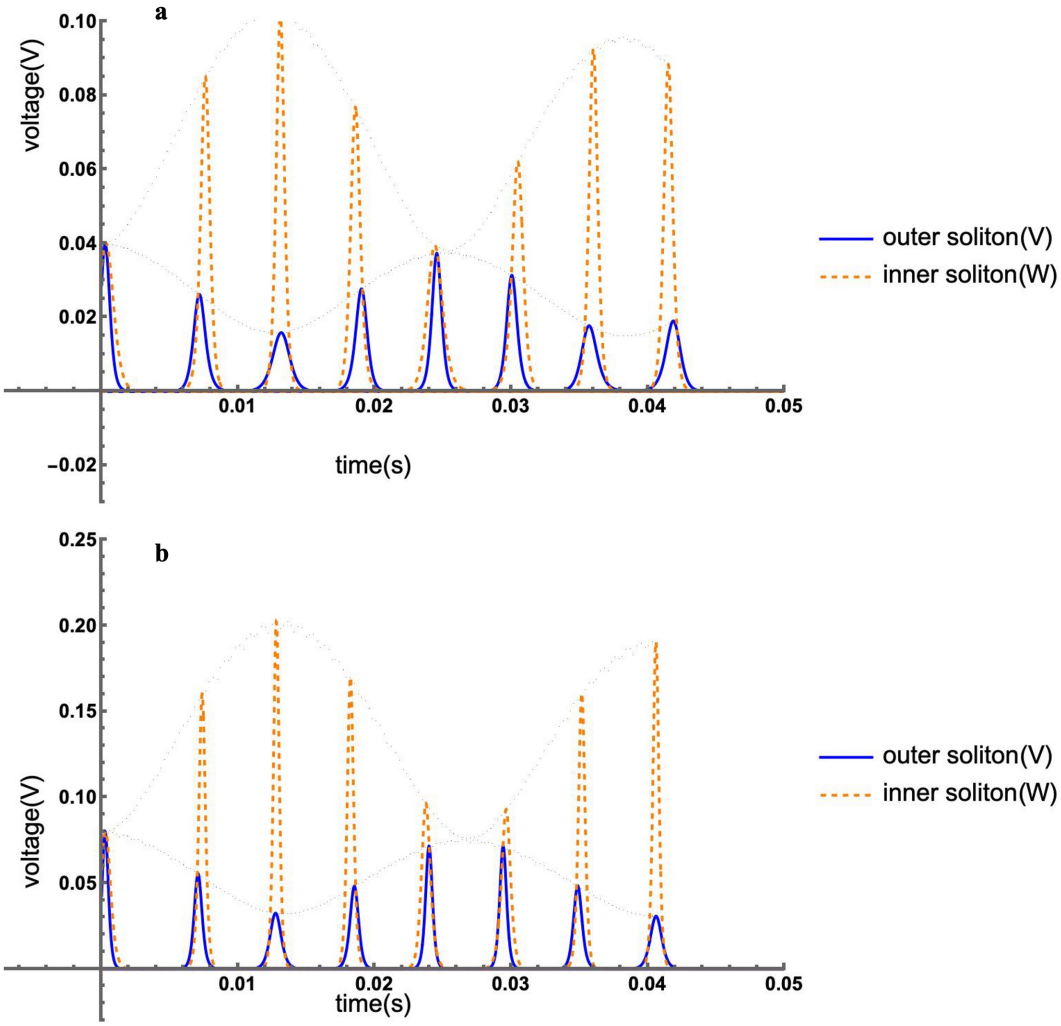

Figure 5. Effects of asymmetric ionic layer parameters on soliton propagation along MTs. (a) Input voltage 0.04 V. (b) Input voltage 0.08 V. Voltage signal solutions $V(x,t)$ (outer) and $W(x,t)$ (inner) are shown for asymmetric condensed layer parameter values different to those in Fig. 1. The black dotted line indicates the soliton amplitude peak oscillation.

Moreover, we characterized the attenuation of the soliton amplitudes. We calculated the damping parameter γ_0 (see equations 19-22) using an exponential fitting curve $Ae^{-\gamma_0\tau}$ and the aforementioned model parameter values. The fitting results are presented in Fig. 4. The location of the soliton peaks are displayed in red points as a function of the dimensionless time τ, obtaining a value of $\gamma_0 = 0.0012$. This low value means the solitons take 0.84 seconds to reduce their amplitudes by ~37%.

We further examined the effects of the coupling and resistivity terms on the soliton oscillation frequency and amplitude by changing the model parameter values used previously to calculate the voltage signal solutions $V(x,t)$ and $W(x,t)$. In Fig. 5-a, we display the results obtained for the MT model parameter values $M_1 = 0$, $M_2 = 1.403$, $M_3 = 0$, $M_4 = 2.201$, $N_1 = 0.0013$, $N_2 = 0$, $N_3 = 0.0024$, $N_4 = 0$, $F_1 = 0$, and $F_2 = 0$; whereas, in Fig. 5-b, we show the results obtained for $M_1 = 0$, $M_2 = 0.937$, $M_3 = 0$, $M_4 = 1.443$,

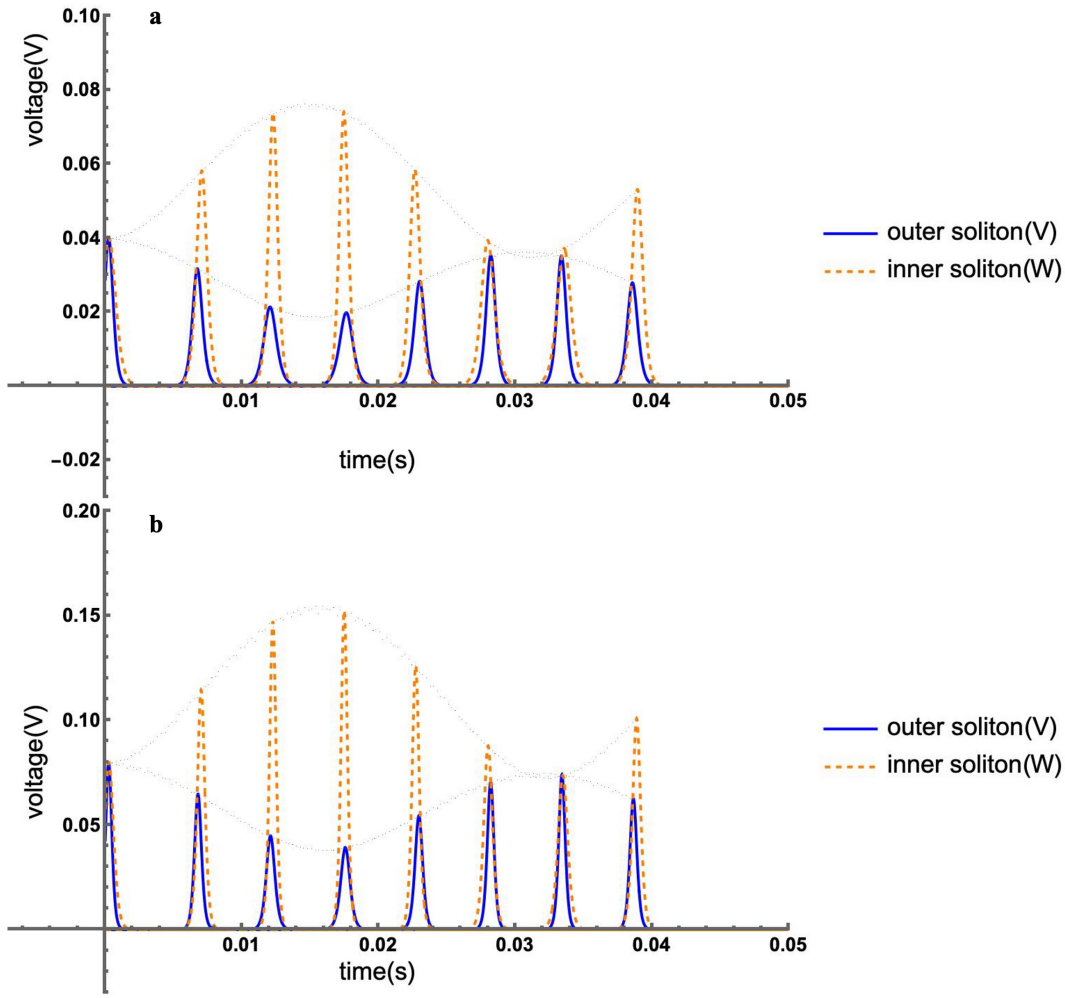

Figure 6. Effects of symmetric ionic layer parameters on soliton propagation along MTs. (a) Input voltage 0.04 V. (b) Input voltage 0.08 V. Voltage signal solutions $V(x,t)$ (outer) and $W(x,t)$ (inner) are shown for symmetric condensed ionic layer parameters. The black dotted line marks the soliton amplitude peak oscillation.

$N_1 = 0.0011$, $N_2 = 0$, $N_3 = 0.0021$, $N_4 = 0$, $F_1 = 0$, and $F_2 = 0$ (see equations 11 and 12 for more details on these parameters). Comparison between the results presented in Fig. 1 and 5 reveals a dominant role of the coupling terms M_2 and M_4 appearing in the soliton KdV equations 9 and 10 on the soliton oscillation. Additionally, the soliton amplitudes are higher in Fig. 5 than in Fig. 1 because we have set some resistivity terms in the soliton KdV equations equal to zero.

Finally, we elucidated the role of the asymmetry between the outer and inner condensed ionic layer parameters on the time evolution of the voltage signal solutions. Figures 6-a and 6-b display the results for the set of symmetric parameter values: $M_1 = M_2 = M_3 = M_4 = 1.404$, $N_1 = N_2 = N_3 = N_4 = 0.0015$, $F_1 = F_2 = -0.047$, and $M_1 = M_2 = M_3 = M_4 = 0.937$, $N_1 = N_2 = N_3 = N_4 = 0.0010$, $F_1 = F_2 = -0.029$, respectively. Comparison between the results shown in Fig. 6 and 1 demonstrates a substantial impact of the condensed ionic layer model parameter values on the soliton oscillation frequencies, velocities, and

amplitudes.

Discussion

This article introduces an innovative multi-scale electrokinetic model that accounts for the atomistic details of the protein molecular structure and biological environment and explains the electrical oscillations propagating along MTs (Fig. 8-10). We propose that condensed ionic layers on the outer and inner surfaces of the MT form a pair of asymmetric coupled nonlinear inhomogeneous electrical transmission lines. The formulation includes non-trivial contributions to the ionic electrical conductivity and capacitance from the diffuse part of the tubulin's EDL. It also accounts for the asymmetric outer and inner surface charge densities, the hollow size, a low dielectric constant in the condensed layers ($\varepsilon \sim 9$) generated by the high polarization of immobile water molecules, and a lower relative dielectric constant ($\varepsilon_2 \sim 2$) between the outer and inner surfaces coming from the internal MT molecular structure properties (see equations S.1–S.11 in the supplementary document for more details). We utilize this tubulin characterization in an outer and inner nonlinear inhomogeneous transmission line prototype model to account for the tubulin–tubulin interactions, dissipation, and damping perturbations along the filament length. As a unique feature, a voltage-dependent nanopore that connects the outer and inner electrical transmission lines is considered explicitly to account for the ionic current through the lumen, the electrical energy transfer between the inner and outer surfaces, and, consequently, the experimentally observed electrical signal amplification, oscillations, and rectification (see Fig. 7). The approach is a powerful tool to determine the effects of electrolyte conditions and voltage stimulus on the electrical impulse shape, attenuation, oscillations, and propagation velocity.

The present model captures the core features of microtubule electrodynamics through coupled nonlinear transmission lines while also integrating emerging evidence that MT assemblies behave as memristive systems. Our prior work demonstrated that voltage-clamped, non-oscillating MT sheets exhibit both a small, saturating voltage-dependent capacitance and a non-saturating, time- and voltage-dependent resistance—hallmarks of memristive devices [23]. Within the framework of the current model, the voltage dependence of the nanopore resistance closely resembles the conservation function in memristive theory. In contrast, the bell-shaped nonlinear capacitance mimics the memory function associated with voltage-induced conformational gating. Together, these elements provide a biophysical basis for the emergence of history-dependent electrical behavior and sustained oscillations. The resulting circuit behaves as a nonlinear memristive capacitor embedded in a transmission network, where the frequency of the oscillations is stabilized around 39 Hz due to the saturation of both the resistance and capacitance components within the functional voltage range. Moreover, including nonlinear, state-dependent elements in the model offers a plausible pathway for frequency diversity through adaptive changes in internal parameters or ionic environments, potentially linking microtubule-based electrodynamics to the full spectrum of EEG oscillatory behavior. This formulation supports the hypothesis that intracellular MTs could be intrinsic bioelectronic memory elements and signal processors within neurons.

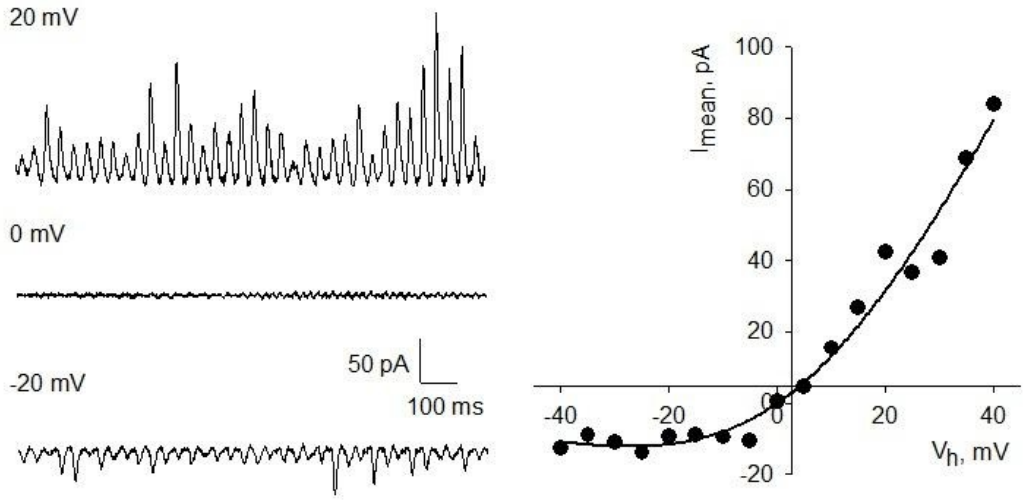

Figure 7. Electrical oscillations and rectification obtained in a two-dimensional MT structure, as described in reference [5]. (Left) Representative tracings of the effect of the input voltage, as indicated, on the MT sheet current oscillations. (Right) Current-to-voltage relationship obtained from integrated, mean currents of individual experiments without any changes in electrochemical gradient.

Our numerical results predict oscillatory electrical signal impulses propagation along the MT in the form of localized ionic wave packages, called leapfrogging solitons, for the range of voltage stimulus and electrolyte solutions typically present in in-vitro experimental conditions [5, 6, 7] (Fig. 1-4). While the outer soliton peak increases, the inner decreases, and vice versa (Fig. 1). Likewise, the velocity of the increasing soliton increases, whereas the velocity of the attenuating soliton decreases, and vice versa. Additionally, the outer and inner soliton velocities oscillate in opposite phases such that when one soliton accelerates, the other decelerates (Fig. 2). This oscillation frequency reproduces experimental measurements (Fig. 3). Moreover, solitons slightly reduce their velocities and amplitudes with each oscillation cycle due to damping and dissipation perturbations (Fig. 4). This feature is characteristic of leapfrogging systems [21, 22]. The electrical energy transferred from the leading soliton to the trailing soliton through the nanopores accelerates the trailing soliton by gaining kinetic energy. It decelerates the leading soliton by reducing kinetic energy. As a result, they shift their position at every oscillation cycle so that the leading one becomes the trailing soliton and vice versa. At lower input voltage, the average velocity and amplitude are lower; however, the velocity oscillation range is higher. Conversely, the average velocity and amplitude are higher at higher input voltage. Additionally, the velocity and amplitude changes are more pronounced in the inner soliton than in the outer one. This leapfrogging electrokinetic motion allows MTs to transmit electrical signals to relatively large distances with minimum power loss [21].

Further examination of the electrical signal propagation along MTs revealed a dominant role of the coupling terms between the outer and inner solitons on the oscillation frequency. In contrast, the diffusion

and damping terms mainly affected the soliton amplitudes (Fig. 5). We noticed that the asymmetric characterization considered between the outer and inner condensed ionic layers of the MT plays a key role in the soliton solutions (Fig. 1 and 6). It generated more prominent outer and inner soliton amplitude changes and a slightly higher oscillation frequency than those obtained from a symmetric condensed ionic layer model.

Moreover, we presented convenient, simple, easy-to-evaluate approximate analytical soliton solutions to characterize electrical signal propagation along MTs qualitatively .

It is worth highlighting a unique attribute of the proposed MT approach: the voltage-dependent nanopore resistance model, which allowed us to incorporate an equivalent transistor model for signal amplification in MT [4]. Its value was adjusted to reproduce the experimental oscillation frequencies [5, 6, 7] (Fig. 3). As a result, it shows a voltage dependence of the nanopore resistance. (Fig. 11). This type of rising resistance with voltage can be explained with voltage dependent blocking [25]. The resulting current-voltage relationship exhibits outward rectification(Fig. 11-b), as has been experimentally demonstrated in microtubule-based systems [5, 6].

Integrating the transistor-like properties in MTs has profound implications for intracellular communication and bioelectronic applications. The dynamic modulation of the ionic conductance suggests that MTs could participate in intracellular computation, signal amplification, and frequency-dependent processing similar to artificial bioelectronic circuits. By explicitly incorporating the concept of time-variant pore conductance into the electrical oscillation model of MTs, we provide a robust transistor-based framework for understanding their bioelectronic behavior.

The voltage stimulus values used in our studies may also represent in-vivo conditions. For instance, steep transmembrane ion gradients in eukaryotic cells are critical for receiving and processing environmental information. Information is received when some perturbation causes the protein gates in transmembrane ion channels to open. The subsequent flow of ions into or out of the cell along these pre-existing electrochemical gradients can induce local changes and, consequently, electrical potential drops along MTs.

Further extension of the two coupled transmission lines model could be used to investigate electrical signal propagation in higher-order cytoskeleton structures characterized by a network of multiple parallel-coupled electrical transmission lines. Each transmission line can represent a cytoskeleton filament characterized by voltage-dependent (nonlinear) capacitors and resistances to account for ionic flows, as described in this work. Additionally, the coupling parameters model would depend on the specific structures. For instance, a hexagonal transmission line configuration can be used for bundle structures, whereas MT sheets can be modeled as parallel transmission lines in a two-dimensional arrangement. Therefore, this framework can provide the foundation to integrate electrical signal propagation along cytoskeleton structures in neuronal cable-like theories to better understand the electrical activities in neurons.

Overall, the approach bridges the gap between nonlinear electrokinetics and biologically inspired

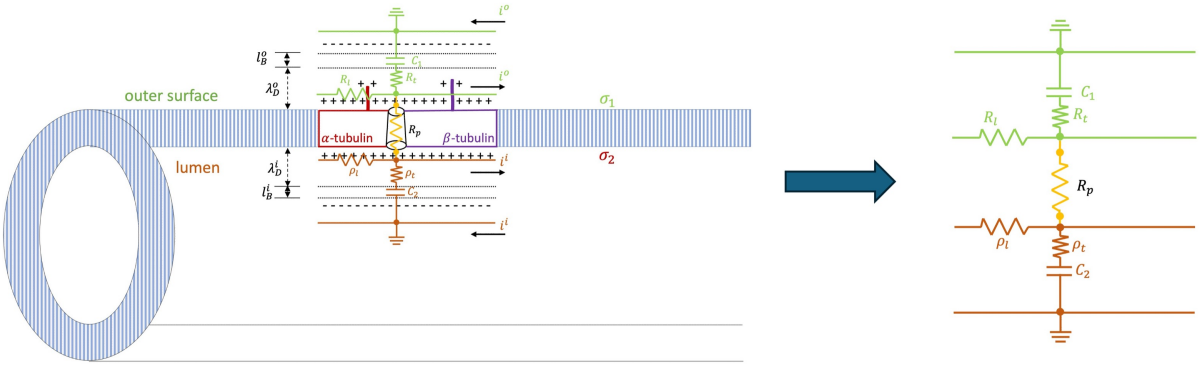

Figure 8. Multi-scale electrokinetic model for microtubules. It represents the outer and inner EDLs as coupled transmission lines (green and brown) connected through nanopores in the microtubule wall (yellow), modeling tubulin as a hollow cylindrical structure.

transistor models, offering new avenues for investigating MT-based information processing and intracellular signal regulation. Indeed, our equivalent circuit representations and governing equations provide a quantitative foundation for future experimental validation and bioelectronic applications. They may help investigate novel direct paths for transporting ions along MTs at relatively more considerable distances, which might be crucial for many electrical processes in localized eukaryotic cell elements [26]. MTs extend electrostatic interactions within the cell, overcoming ionic screening limitations [27] that allow MTs to form part of a cellular-wide electric field network, facilitating long-range signaling. MTs play a critical role in intracellular calcium signaling [28], where localized calcium waves may propagate along MTs, affecting processes like MT depolymerization during cell division. These waves travel faster than diffusion, suggesting an efficient mechanism for cellular regulation [13]. MTs are linked to gamma brain waves (30-100 Hz) in the brain, which are important for cognitive functions like memory, perception, and learning [5].

Methods

We introduce a novel hollow cylindrical biomolecule model for tubulins (Fig. 8) and a two coupled electrical transmission lines prototype model (Fig. 9) to characterize the ionic electrical conductivity of MTs in intracellular aqueous electrolyte solutions. This approach expands upon the transmission line framework developed for our actin filament model [15].

We retrieved the MT molecular structure information using the cryo-electron microscopy model 3j2u posted on the protein data bank [29]. It provides a detailed molecular characterization, including the amino acid sequence and the number and type of residues exposed to the electrolyte. This uncharged molecular structure in pdb format is uploaded into CSDFTS software [30] to assign atomic charges and sizes, add hydrogens, optimize the hydrogen bonding network, and renormalize atomic charges of the residues exposed to the surface due to pH effects (protonation/deprotonation process). Molecular structure analysis indicated that the single MT resembles a long, hollow cylindrical biomolecule with an outer

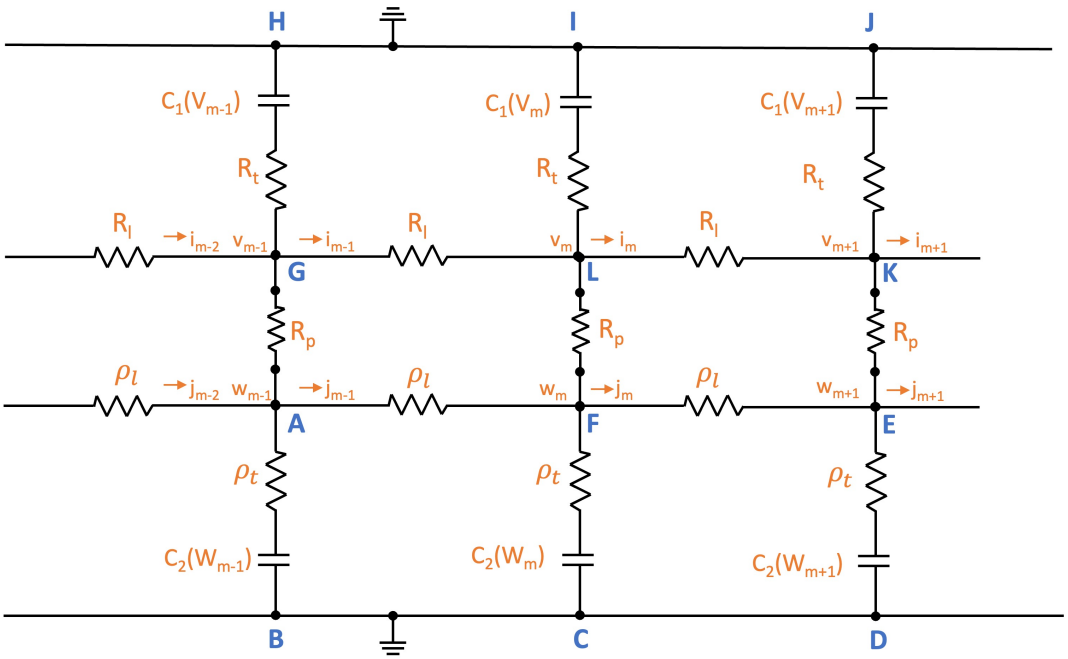

Figure 9. Ladder transmission lines model. The electric circuit unit cell represents an elementary ring of tubulin dimers shown in Fig. 8.

diameter of approximately 25 nm, a wall thickness of about 5 nm, and a hollow central core measuring around 15 nm in diameter. The number of protofilaments in MTs typically ranges from 10 to 15 in-vitro, with 13 being the most common (Fig. 10).

In this context, we modeled MTs as polyelectrolytes with negative charges uniformly distributed on the tubulin surface with an approximate charge ratio of 2:1 between the outer and inner surfaces [14]. We characterize each transmission line's electrical and conductive properties using the hollow cylindrical biomolecule model for tubulin dimers, Ohm's law, Navier-Stokes, and Poisson's theories (see supplementary document). The formulation includes non-trivial contributions to the ionic electrical conductivity and capacitance from the diffuse part of the EDLs. It also accounts for the asymmetric outer and inner surface charge densities, the hollow size, a low dielectric constant in the condensed layers ($\varepsilon \sim 9$) generated by the high polarization of the immobile water molecules, and a lower relative dielectric constant ($\varepsilon_2 \sim 2$) between the outer and inner surfaces coming from the internal MT molecular structure properties. Specific considerations on the outer and inner transmission lines and their coupling interaction via nanopores are provided below. More details on these calculations can be found in the supplementary document.

Outer Transmission Line Model

Here, we highlight the modifications and extensions done on a single transmission line model for actin filaments [15] to characterize the outer transmission lines for MTs. We replace the elementary circuit unit of an actin monomer with an elementary ring of 13 dimers of a radius of 12.5 nm and length of $l = 8\,nm$.

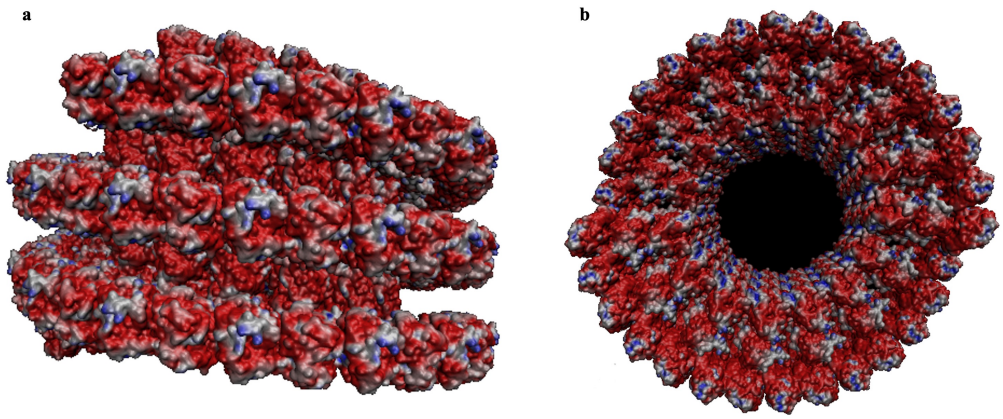

Figure 10. MT molecular structure and surface charge distribution. (a) Longitudinal view. (b) Cross-section view. Cryo-electron microscopy data (PDB ID: 3j2u) were used to model the microtubule structure and surface charge distribution. Red indicates negative charges, blue positive charges, and white neutral regions.

Similarly, the EDL capacitor accounts for a nonlinear condensed ionic cloud in the radial direction on the MT that changes with applied voltage and contributes to the nonlinearity of the electrical impulse. Unlike G-actin monomers, tubulins have short, negatively charged C-terminal tubulin tails (TTs) that extend 4–5 nm from the microtubule surface. Since TTs undergo shrinking [12, 13, 14] and thermal oscillations [20], they contribute to MT nonlinearity. These properties are considered using the nonlinear charge condensation

$$Q_m = C_1^0 V_m \left(1 - b_1 V_m\right) \tag{1}$$

where V_m represents the outer unit circuit voltage, and C_1^0 stands for the linear part of the capacitance. The nonlinear capacitance calculations performed for G-actin proteins [15] cannot be extended to tubulins because they are valid for solid cylinders only. Instead, here we solved the linearized Poisson Boltzmann equation for the electric potential of an infinite long tubular cylinder to get the value of the linear capacitance for the outer line $C_1^0 = 2.303 \times 10^{-16}\,F$ (see supplementary document for more details). In this model, the small nonlinear parameter b_1 is unknown since it represents the change in capacitance with voltage, coming from the outer condensed ionic cloud and TTs. It is assumed to be a free parameter of the model, and its value is set equal to $b_1 = 0.06\,V^{-1}$, which is small compared to the voltage stimulus range considered in these studies.

Another MT feature considered in this model is the dispersion of the electrical impulse generated by the structural periodicity manifest in the tubulin dimers arrangement. Meanwhile, the longitudinal and transversal resistors account for the losses in the transmission media. By combining the electric potential solution for a tubular cylinder and the electrokinetic ionic current expressions coming from Ohm's law and Poisson's and Navier-Stokes' equations, we calculated the longitudinal resistance for the outer line,

yielding a value of $R_l = 5.845 \times 10^6\,\Omega$ (see supplementary document for more details). In contrast, the transversal resistance calculations performed for G-actin proteins [15] cannot be extended to tubulins because they do not account for MT nanopores and TTs, which is not an obstacle for single-transmission line models [14] since the transversal resistance is supposed to be very high. The leakage of ionic currents through the depleted layer can be ignored. However, in the leapfrogging model of coupled two transmission lines, current leakages through the depleted layer and nanopore significantly influence soliton oscillations. Thus, we consider a high value for the outer transversal resistance $R_t = 7.792 \times 10^{14}\,\Omega$, which is in the same order as the pore resistance. Additionally, we set the outer impedance to $Z_1 = 1.862 \times 10^{11}\,\Omega$, and the inductance is so small (of the order of $\sim 10^{-16}\,H$) compared to the other impedance components that we ignored its effect [12, 13, 14].

Inner Transmission Line Model

Figure 9 shows that the inner electrical transmission line mirrors the outer transmission line described above but has different (asymmetric) electric circuit parameter values. Here, we remark on the main changes to the outer transmission line calculations to characterize the electric circuit for the lumen. We consider a negatively charged inner surface with a surface charge density ratio of 1:4 to the outer surface [31]. We define the nonlinear capacitance of the inner line as

$$q_m = C_2^0 W_m (1 + b_2 W_m) \tag{2}$$

where W_m represents the inner unit circuit voltage, and $C_2^0 = 1.357 \times 10^{-16}\,F$ represents the inner linear capacitance. We noticed that C_1^0 is greater than C_2^0 since the outer condensed ionic cloud thickness is four times greater than the inner one. Additionally, b_2 denotes a small lumen nonlinearity parameter, which we set equal to $b_2 = 0.03\,V^{-1}$, a lower value than the outer one because there are no TTs in the former. Another essential difference between the outer and inner lines is the nonlinear term sign, which accounts for the opposite polarities of the voltage-dependent capacitors on the two lines [22]. The calculations for the longitudinal resistance of the inner line yielded $\rho_l = 1.810 \times 10^7\,\Omega$. Additionally, we estimated the inner transversal resistance and impedance by $\rho_t = 3.779 \times 10^{14}\,\Omega$ and $Z_2 = 3.126 \times 10^{11}\,\Omega$, respectively.

Incorporating Time-Variant Pore Conductance into the Transistor Model of Microtubule Oscillations

MTs exhibit electrical properties that suggest their role as dynamic conductors of ionic currents. Their structure, characterized by highly charged surfaces and periodic nanopores, enables them to function as biological transmission lines. However, beyond this passive conductive role, experimental observations indicate that MTs amplify electrical signals [4, 11], sustain oscillatory dynamics, and exhibit voltage-dependent behavior [5, 6, 7]. These features suggest a functional analogy to transistors, where the nanopores act as gates regulating the flow of ions in response to external stimuli.

In classical transistors, a small control signal at the gate modulates a larger current between the source

and drain terminals. A similar mechanism is present in MTs, where nanopores' periodic opening and closing control ionic flow across the structure, leading to oscillatory charge dynamics that can be modeled in various transistor frameworks. In a FET model, the nanopores act as gate-controlled conduits for ionic currents, where the electrostatic potential near the pore entrance modulates the conductance. This dynamic regulation of the pore conductance resembles the behavior of a voltage-gated FET, where the local electric field influences the density and mobility of charge carriers. In this case, the drain-source current can be expressed as

$$I_D = I_{D0}\left(1 + \beta V_G + \gamma V_G^2\right) \tag{3}$$

where I_{D0} is the baseline drain current, V_G is the gate voltage (nanopore potential), β is the gate modulation factor (linear term), and γ accounts for higher-order nonlinearities in conductance. The dynamic modulation of ionic charge carrier mobility could also be described as

$$\mu(V_G) = \mu_0(1 + \alpha V_G) \tag{4}$$

where μ_0 is the baseline charge carrier mobility and α describes the dependence of mobility on gate voltage.

In JFETs, a depletion region controls the current. Similarly, in MTs, counterion condensation and depletion within the nanopores modulate the ionic flow, creating a time-dependent gate potential that governs oscillatory conduction. The conductance can be modeled as

$$G_{MT}(t) = G_0 + G_1 e^{(-t/\tau)} + G_p(V_G, t) \tag{5}$$

where G_0 is the baseline conductance, G_1 represents transient gating effects that decay over time with characteristic time constant τ, and $G_p(V_G, t)$ is the voltage- and time-dependent pore conductance.

In a Bipolar Junction Transistor (BJT) analogy, nanopores serve as the base region, where small variations in ionic concentration similar to the base current lead to amplified changes in longitudinal ionic currents (collector-emitter current). The current amplification can be described as

$$I_C = \beta I_B + I_{leak} \tag{6}$$

where I_C is the ionic collector current, β is the current gain, I_B is the base current from nanopore dynamics, and I_{leak} accounts for ionic leakage through the MT walls.

The amplifying function of the MT system can be further characterized by defining an effective β parameter for ion transport

$$\beta_{MT} = \frac{I_{extout}}{I_{extin}} = \frac{G_{extMT} V_{extMT}}{G_{extpore} V_{extpore}} \tag{7}$$

where G_{MT} and V_{MT} represent the total microtubule conductance and voltage, while G_{pore} and V_{pore} capture the localized gating effects of the nanopores.

This amplification mechanism suggests that small local perturbations in ionic concentrations at the nanopores could lead to significant long-range signal propagation, similar to transistor-based amplification in electronic circuits.

Coupling to Leapfrogging Transmission Lines

We consider that the outer and inner electrical transmission lines are coupled through nanopores with a diameter of about 1.7 nm [32]. The nanopores are permeable to counterions from the ionic clouds on the inner and outer surfaces [14, 19] and impermeable to anions [19]. Thus, counterions are exchanged between the inner and outer transmission lines through the nanopores. Voltage-clamp experimental data on MTs show that the oscillating current frequency (~39 Hz) does not depend on the voltage stimulus [5, 6, 7]. This result implies that nanopores can be characterized by a voltage-dependent nonlinear resistance $R_p(V)$ [13], directly influencing the coupled soliton dynamics. This introduces a self-regulatory mechanism where the interplay between ion accumulation and depletion cycles at the pores creates a time-dependent gating effect. The result is a leapfrogging behavior, where ionic solitons continuously overtake each other, similar to the oscillatory charge redistribution in a transistor circuit [21, 22].

To determine $R_p(V)$, we kept all the circuit parameters in Fig. 1 fixed, and adjusted pore resistance values in the input voltage range between 0.01V and 0.1V to reproduce the experimental oscillation frequency. Figure 11-a displays our results. The corresponding I-V curve, computed using a reversal potential of 5ămV to reflect the slight asymmetry between the intra- and extra-microtubule ion concentrations, is shown in fig. 11-b. The data shows good fit with 2S3B energy model for ion permeation through the pore[5, 25]. The I–V relationship is given by the following expression

$$I = zFQexp\left(-G_{23}+G_3+G_2\right)A\left\{\frac{exp\left[\left(d_2+2d_1\right)\frac{zF}{RT}V\right]}{\left[S^+\right]_o}-\frac{exp\left[-\left(d_2+2d_3\right)\frac{zF}{RT}V\right]}{\left[S^+\right]_i}\right\} \tag{8}$$

where $[S^+]_o$ and $[S^+]_i$ are the concentrations of permeable ion in the MT outer and intra environment, respectively, V is the potential, F is the Faraday constant, R is the universal gas constant, T is the temperature, z is the ion valence, and Q is a prefactor encompassing the transition rate constants between pore states. Also, G_{23} is the peak energy, G_2 and G_3 are the well energies, and d_1, d_2, and d_3 are the three electrical distances. In our fitting, the optimal parameter values are $A = 2.21$, $G_2/G_3 = -0.70$, $G_{23} = -0.66$, $d_1 = 0.04$,$d_2 = 0.03$, and $d_3 = 0.55$. These values are qualitatively similar to the values obtained in fitting voltage clamp experimental data [5].

Transmission Lines Model Solution

We solved the coupled electrical transmission lines following the procedure introduced in our model for actin filaments [15]. Applying Kirchoff's rules to the unit cell number m, we obtained equations S.25 and S.26 provided in the supplementary document (see Fig. 9). We used the notation $V_m = Z_1^{1/2}U_m$

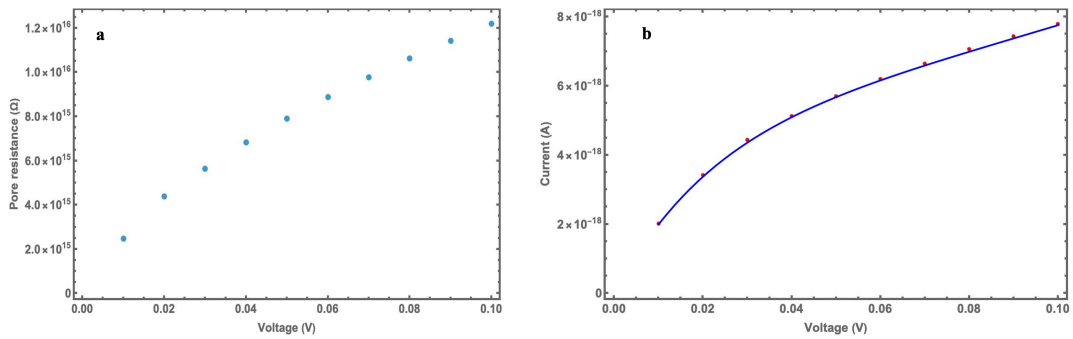

Figure 11. Voltage-dependent nanopore resistance model. a) The pore resistance $R_p(V)$ is calculated for input voltages ranging from 0.01 V to 0.1 V, keeping the other circuit parameters fixed. b) The corresponding current-volrage (I-V) curve shows outward rectification. Red dots represent the calculated data points, and the blue curve corresponds to the fit using the 2S3B energy model.

and $W_m = Z_2^{1/2} X_m$ for the outer and inner voltage lines. Since the circuit unit length is much less than the MT length (i.e., the length of the transmission line), voltages and currents in the transmission lines change gradually from one circuit unit to the next. This allowed us to use the continuum approximations $U_m(t) \simeq U(x,t)$ and $X_m(t) \simeq X(x,t)$, and to apply the transformations to the space and time coordinates $\xi = \frac{x}{\beta} - \frac{t}{\alpha}$ and $\tau = \frac{t}{24\alpha}$, with $\alpha = \sqrt{C_1^0 Z_1 C_2^0 Z_2}$ and $\beta = 2l$ (l is the length of the dimer, e.g. 8 nm). Finally, we rescaled the transmission line voltages $U = -\frac{\gamma_1}{24}\Psi$ and $X = \frac{\gamma_2}{24}\Phi$ in equations S.31 and S.32 in the supplementary document, with $\gamma_1 = \frac{3}{b_1 Z_1^{1/2}}$ and $\gamma_2 = \frac{3}{b_2 Z_2^{1/2}}$, to obtain the following two master coupled perturbative KdV equations

$$\frac{\partial \Psi}{\partial \tau} - 6\Psi \frac{\partial \Psi}{\partial \xi} + \frac{\partial^3 \Psi}{\partial \xi^3} = P_1 \tag{9}$$

$$\frac{\partial \Phi}{\partial \tau} - 6\Phi \frac{\partial \Phi}{\partial \xi} + \frac{\partial^3 \Phi}{\partial \xi^3} = P_2 \tag{10}$$

where,

$$P_1 = -M_1 \frac{\partial \Psi}{\partial \xi} + M_2 \frac{\partial \Phi}{\partial \xi} - N_1 \Psi - N_2 \Phi - F_1 \frac{\partial^3 \Psi}{\partial \xi^3} \tag{11}$$

$$P_2 = -M_3 \frac{\partial \Phi}{\partial \xi} + M_4 \frac{\partial \Psi}{\partial \xi} - N_3 \Phi - N_4 \Psi - F_2 \frac{\partial^3 \Phi}{\partial \xi^3} \tag{12}$$

Labels 1 and 2 on P represent the outer and inner transmission lines. The expressions for the parameters N's, M*'s,* and F*'s* in equations 11 and 12 are linked to the electric circuit parameters through the equations S.33 to S.44 in the supplementary document. They yield the following set of parameter values: $M_1 = -2.578$, $M_2 = 1.404$, $M_3 = -1.130$, $M_4 = 2.201$, $N_1 = 0.0013$, $N_2 = 0.0015$, $N_3 = 0.0024$, $N_4 = 0.0005$, $F_1 = -0.107$, $F_2 = -0.047$; and $M_1 = -1.766$, $M_2 = 0.937$, $M_3 = -0.694$, $M_4 = 1.443$, $N_1 = 0.0011$, $N_2 = 0.0010$, $N_3 = 0.0021$, $N_4 = 0.0004$, $F_1 = -0.074$, $F_2 = -0.029$ for 0.04 V and 0.08 V

input voltages respectively. It is worth noting that P_1 and P_2 combine coupling and self-perturbation terms. The first terms on the left of equations 9 and 10 resemble the time-dependent term in Fick's diffusion law. The second and third terms represent the nonlinearity and dispersive contributions arising from the condensed ion cloud in the EDL and the diffuse spreading of ions along the MT, respectively. On the other hand, the first and second terms to the right in equations 11 and 12 represent the electric fields generated by the ions in the outer(inner) and inner(outer) EDLs and resemble the potential gradient term in the Nernst-Plank electrodiffusion equation. The third and fourth terms to the right represent the damping perturbations.

To solve the perturbative KdV equations 9 and 10, we followed a similar procedure introduced in our actin filament article [15] and the leapfrogging articles [21, 22]. The exact soliton solutions for $P_1 = P_2 = 0$ correspond to the homogenous KdV equations given by

$$\Psi = -2\kappa_1^2 \mathrm{sech}^2 y_1 \tag{13}$$

$$\Phi = -2\kappa_2^2 \mathrm{sech}^2 y_2 \tag{14}$$

where $y_1 = \kappa_1 (\xi - \theta_1)$ and $\theta_1 = 4\kappa_1^2 \tau$, $y_2 = \kappa_2 (\xi - \theta_2)$ and $\theta_2 = 4\kappa_2^2 \tau$.

According to the adiabatic perturbation theory [24], the perturbations P_1 and P_2 modify these homogenous solutions, which is accounted for by introducing time-dependence on the amplitudes $\kappa_i \to \kappa_i(\tau)$ and solving the following integrodifferential equations

$$\frac{d\kappa_i}{d\tau} = -\frac{1}{4\kappa_i} \int_{-\infty}^{+\infty} P_i \mathrm{sech}^2 y_i dy_i \tag{15}$$

$$\frac{d\theta_i}{d\tau} = 4\kappa_i^2 - \frac{1}{4\kappa_i^3} \int_{-\infty}^{+\infty} P_i (y_i + \frac{1}{2}\sinh 2y_i) \mathrm{sech}^2 y_i dy_i \tag{16}$$

Substitution of equations 11, 12, 13, and 14 into equations 15 and 16 yielded the four coupled first-order asymmetric ordinary differential equations S.47, S.50, S.57, and S.58. We solved these equations numerically using Mathematica software (see the supplementary document).

As a first approach, we have numerically solved the coupled ODE system–equations for multiple values of the involved parameters and concluded that the parameters M_1, M_3, N_2, N_4, F_1, and F_2 change the soliton amplitudes but they weakly affect their oscillation frequency. Thus, we neglected these parameters and linearized the coupled ODE system–equations for small $\Delta\theta$ and $\Delta\kappa$ to obtain equations S.59-S.64. These coupled equations were solved in the supplementary document to obtain an approximate analytical expression for the solitons oscillation frequency. In doing so, we got the following damped oscillatory equation

$$\frac{\partial^2 \Delta\theta}{\partial \tau^2} = -2\gamma_0 \frac{\partial \Delta\theta}{\partial \tau} - \omega_0^2 \Delta\theta \tag{17}$$

where

$$\gamma_0 = \frac{1}{3}N, \qquad \omega_0^2 = \frac{8A}{15}\left(M_2+M_4\right)\kappa^3, \qquad \text{and} \qquad A = 8\kappa + \frac{2}{45\kappa}\left(30+\pi^2\right)\left(M_2+M_4\right). \tag{18}$$

We considered $\kappa_1 = \kappa + \lambda_1$, $\kappa_2 = \kappa + \lambda_2$, $\Delta\lambda = \lambda_1 - \lambda_2$ and $\Delta\theta = \theta_1 - \theta_2$, and $N_1 = N_3 = N$.

Using the initial conditions $\Delta\theta\left(\tau = 0\right) = \Delta\theta_0$, and $\Delta\theta_0^{'} = \frac{\partial\Delta\theta}{\partial\tau}|_{\tau=0} = -\left(M_2 - M_4\right) + A\Delta\lambda_0$, we get the following analytic solution for the soliton phase difference

$$\Delta\theta = e^{-\gamma_0\tau}\left[\alpha_1\cos\left(f\tau\right) + \beta_1\sin\left(f\tau\right)\right] \tag{19}$$

where $f = \sqrt{\omega_0^2 - \gamma_0^2}$, $\alpha_1 = \Delta\theta_0$, and $\beta_1 = \frac{\Delta\theta_0^{'} + \Delta\theta_0\gamma_0}{\sqrt{\omega_0^2 - \gamma_0^2}}$.

Similarly, the following damped oscillatory equation for the amplitude difference is obtained

$$\frac{\partial^2\Delta\lambda}{\partial\tau^2} = D - 2\gamma_0\frac{\partial\Delta\lambda}{\partial\tau} - \omega_0^2\Delta\lambda \tag{20}$$

where $D = \frac{8}{15}\left(M_2+M_4\right)\left(M_2-M_4\right)\kappa^3$. Using $\Delta\lambda = \Delta\kappa + \frac{D}{\omega_0^2}$, we can rewrite the previous equation as follows

$$\frac{\partial^2\Delta\kappa}{\partial\tau^2} = -2\gamma_0\frac{\partial\Delta\kappa}{\partial\tau} - \omega_0^2\Delta\kappa \tag{21}$$

As a result, the analytic solution can be expressed as

$$\Delta\kappa = e^{-\gamma_0\tau}\left[\alpha_2\cos\left(f\tau\right) + \beta_2\sin\left(f\tau\right)\right] \tag{22}$$

where $\alpha_2 = \Delta\kappa_0$, $\beta_2 = \frac{\Delta k_0^{'} + \Delta k_0\gamma_0}{\sqrt{\omega_0^2 - \gamma_0^2}}$, and the initial conditions are given by $\Delta\kappa_0 = \Delta\lambda_0 - \frac{D}{\omega_0^2}$, and $\Delta k_0^{'} = \frac{\partial\Delta\kappa_0}{\partial\tau} = \frac{\partial\Delta\lambda_0}{\partial\tau} = -\frac{8}{15}\left(M_2+M_4\right)\kappa^3\Delta\theta_0 - \frac{2}{3}N\Delta\lambda_0$.

References

1. Dustin, P. *Microtubules* (Springer Berlin Heidelberg, 1978).

2. Tuszyński, J. A. *et al.* Molecular dynamics simulations of tubulin structure and calculations of electrostatic properties of microtubules. *Math. Comput. Model.* **41**, 1055–1070, DOI: https://doi.org/10.1016/j.mcm.2005.05.002 (2005).

3. Minoura, I. & Muto, E. Dielectric measurement of individual microtubules using the electroorientation method. *Biophys. J.* **90**, 3739–3748, DOI: https://doi.org/10.1529/biophysj.105.071324 (2006).

4. Priel, A., Ramos, A. J., Tuszynski, J. A. & Cantiello, H. F. A biopolymer transistor: Electrical

amplification by microtubules. *Biophys. J.* **90**, 4639–4643, DOI: https://doi.org/10.1529/biophysj.105.078915 (2006).

5. Cantero, M. d. R., Perez, P. L., Smoler, M., Villa Etchegoyen, C. & Cantiello, H. F. Electrical oscillations in two-dimensional microtubular structures. *Sci. Reports* **6**, 27143, DOI: https://doi.org/10.1038/srep27143 (2016).

6. Cantero, M. d. R., Villa Etchegoyen, C., Perez, P. L., Scarinci, N. & Cantiello, H. F. Bundles of brain microtubules generate electrical oscillations. *Sci. Reports* **8**, 11899, DOI: https://doi.org/10.1038/s41598-018-30453-2 (2018).

7. Gutierrez, B. C., Cantiello, H. F. & Cantero, M. D. R. The electrical properties of isolated microtubules. *Sci. Reports* **13**, 10165, DOI: https://doi.org/10.1038/s41598-023-36801-1 (2023).

8. Manning, G. S. Counterion condensation on charged spheres, cylinders, and planes. *The J. Phys. Chem. B* **111**, 8554–8559, DOI: https://doi.org/10.1021/jp0670844 (2007).

9. Manning, G. S. Limiting laws and counterion condensation in polyelectrolyte solutions I. colligative properties. *The J. Chem. Phys.* **51**, 924–933, DOI: https://doi.org/10.1063/1.1672157 (1969).

10. Manning, G. S. The molecular theory of polyelectrolyte solutions with applications to the electrostatic properties of polynucleotides. *Q. Rev. Biophys.* **11**, 179–246, DOI: https://doi.org/10.1017/S0033583500002031 (1978).

11. Priel, A. & Tuszyński, J. A. A nonlinear cable-like model of amplified ionic wave propagation along microtubules. *EPL (Europhysics Lett.* **83**, 68004, DOI: https://doi.org/10.1209/0295-5075/83/68004 (2008).

12. Satarić, M. V., Ilić, D. I., Ralević, N. & Tuszyński, J. A. A nonlinear model of ionic wave propagation along microtubules. *Eur. Biophys. J.* **38**, 637–647, DOI: https://doi.org/10.1007/s00249-009-0421-5 (2009).

13. Satarić, M. V., Sekulić, D. & Živanov, M. Solitonic ionic currents along microtubules. *J. Comput. Theor. Nanosci.* **7**, 2281–2290, DOI: https://doi.org/10.1166/jctn.2010.1609 (2010).

14. Sekulić, D. L., Satarić, B. M., Tuszyński, J. A. & Satarić, M. V. Nonlinear ionic pulses along microtubules. *The Eur. Phys. J. E* **34**, 49, DOI: https://doi.org/10.1140/epje/i2011-11049-0 (2011).

15. Hunley, C., Uribe, D. & Marucho, M. A multi-scale approach to describe electrical impulses propagating along actin filaments in both intracellular and in vitro conditions. *RSC Adv.* **8**, 12017–12028, DOI: https://doi.org/10.1039/C7RA12799E (2018).

16. Hunley, C., Mohsin, M. & Marucho, M. Electrical impulse characterization along actin filaments in pathological conditions. *Comput. Phys. Commun.* **275**, 108317, DOI: https://doi.org/10.1016/j.cpc.2022.108317 (2022).

17. Sekulic, D. & Sataric, M. An improved nanoscale transmission line model of microtubule: The effect of nonlinearity on the propagation of electrical signals. *Facta universitatis - series: Electron. Energ.* **28**, 133–142, DOI: https://doi.org/10.2298/FUEE1501133S (2015).

18. Ndjomatchoua, F. T., Tchawoua, C., Kakmeni, F. M. M., Le Ru, B. P. & Tonnang, H. E. Z. Waves transmission and amplification in an electrical model of microtubules. *Chaos: An Interdiscip. J. Nonlinear Sci.* **26**, 053111, DOI: https://doi.org/10.1063/1.4952573 (2016).

19. Freedman, H. *et al.* Model of ionic currents through microtubule nanopores and the lumen. *Phys. Rev. E* **81**, 051912, DOI: https://doi.org/10.1103/PhysRevE.81.051912 (2010).

20. Priel, A., Tuszynski, J. A. & Woolf, N. J. Transitions in microtubule C-termini conformations as a possible dendritic signaling phenomenon. *Eur. Biophys. J.* **35**, 40, DOI: https://doi.org/10.1007/s00249-005-0003-0 (2005).

21. Akem, N. A., Dikandé, A. M. & Essimbi, B. Z. Leapfrogging of electrical solitons in coupled nonlinear transmission lines: effect of an imperfect varactor. *SN Appl. Sci.* **2**, 21, DOI: https://doi.org/10.1007/s42452-019-1740-5 (2019).

22. Akem, N. A., Akong Ngate, L., Dikandé, A. M. & Essimbi, B. Z. Leapfrogging dynamics of interacting solitons in weakly coupled nonlinear transmission lines. *SN Appl. Sci.* **1**, 552, DOI: https://doi.org/10.1007/s42452-019-0555-8 (2019).

23. Cantero, M. d. R., Perez, P. L., Scarinci, N. & Cantiello, H. F. Two-dimensional brain microtubule structures behave as memristive devices. *Sci. Reports* **9**, 12398, DOI: https://doi.org/10.1038/s41598-019-48677-1 (2019).

24. Kivshar, Y. S. & Malomed, B. A. Dynamics of solitons in nearly integrable systems. *Rev. Mod. Phys.* **61**, 763–915, DOI: https://doi.org/10.1103/RevModPhys.61.763 (1989).

25. Hille, B. & Schwarz, W. Potassium channels as multi-ion single-file pores. *The J. general physiology* **72**, 409–442, DOI: 10.1085/jgp.72.4.409 (1978).

26. Frieden, B. R. & Gatenby, R. A. Signal transmission through elements of the cytoskeleton form an optimized information network in eukaryotic cells. *Sci. Reports* **9**, 6110, DOI: https://doi.org/10.1038/s41598-019-42343-2 (2019).

27. Gagliardi, L. Microscale electrostatics in mitosis. *J. Electrost.* **54**, 219–232, DOI: https://doi.org/10.1016/S0304-3886(01)00155-3 (2002).

28. Hepler, P. K. Calcium: A central regulator of plant growth and development. *The Plant Cell* **17**, 2142–2155, DOI: https://doi.org/10.1105/tpc.105.032508 (2005).

29. Asenjo, A. B. *et al.* Structural model for tubulin recognition and deformation by kinesin-13 microtubule depolymerases. *Cell Reports* **3**, 759–768, DOI: https://doi.org/10.1016/j.celrep.2013.01.030 (2013).

30. Marucho, M. A java application to characterize biomolecules and nanomaterials in electrolyte aqueous solutions. *Comput. Phys. Commun.* **242**, 104–119, DOI: https://doi.org/10.1016/j.cpc.2019.03.022 (2019).

31. Shen, C. & Guo, W. Ion permeability of a microtubule in neuron environment. *The J. Phys. Chem. Lett.* **9**, 2009–2014, DOI: https://doi.org/10.1021/acs.jpclett.8b00324 (2018).

32. Li, H., DeRosier, D. J., Nicholson, W. V., Nogales, E. & Downing, K. H. Microtubule structure at 8 Å resolution. *Structure* **10**, 1317–1328, DOI: https://doi.org/10.1016/S0969-2126(02)00827-4 (2002).

Acknowledgments

M. Mohsin and Dr. M. Marucho thank Dr. Dikande Alain Moise and Dr. Nkongho Achere Akem for sharing calculations of the leapfrogging approach and Dr. Vadim Warshavsky for his contribution to the Poisson's equation solution for MTs.

Funding

This work was partially supported by the National Institutes of Health under grant number 1SC2GM112578 (M. Marucho).

Author Contributions

M. Marucho designed the research; M. Mohsin and M. Marucho developed the mathematical model and performed simulations; M. Mohsin prepared all the figures corresponding to the model and numerical results; H. Cantiello and M. d.R. Cantero provided experimental validation and prepared Fig. 7; M. Mohsin and M. Marucho wrote the main manuscript text; all authors reviewed and edited the manuscript.

Data Availability

The datasets used and/or analysed during the current study are available from the corresponding author on reasonable request.

Competing Interests

The authors declare no competing interests.

Additional Information

Additional information is provided in the supplementary document.

Figure Legends

Figure **1** | Soliton-like voltage propagation along the MT under asymmetric ionic conditions.Time evolution of the outer voltage $V(x,t)$ and inner (lumen) voltage $W(x,t)$ for input voltages of 0.04 V (a) and 0.08 V (b) at increasing positions along the microtubule: x = 0.1 , 2.6 , 4.6 , 6.6 , 8.6 , 10.6 , 12.6 , 14.6 μm. The black dotted line represents the soliton amplitude peak oscillation.

Figure **2** | Soliton propagation velocities along the MT. (a) Input voltage 0.04 V. (b) Input voltage 0.08 V. These results correspond to the soliton-like voltage propagation described in Fig. 1.

Figure **3** | Experimental soliton oscillation frequencies. Current oscillations of Paclitaxel-stabilized isolated MTs. (Left) Current fluctuations at different holding potentials. (Right) Linear–linear plots of the Fourier power spectra obtained from tracings shown on the Left. The fundamental frequencies can be observed on the spectra (Ref. [7]).

Figure **4** | Soliton amplitude attenuation and damping parameter estimation. Exponential fitting of soliton peak amplitudes as a function of dimensionless time τ. (a) Input voltage 0.04 V. (b) Input voltage 0.08 V. Red points represent the soliton peak locations. These results correspond to the soliton-like voltage propagation described in Fig. 1.

Figure **5** | Effects of asymmetric ionic layer parameters on soliton propagation along MTs. (a) Input voltage 0.04 V. (b) Input voltage 0.08 V. Voltage signal solutions $V(x,t)$ (outer) and $W(x,t)$ (inner) are shown for asymmetric condensed layer parameter values different to those in Fig. 1. The black dotted line indicates the soliton amplitude peak oscillation.

Figure **6** | Effects of symmetric ionic layer parameters on soliton propagation along MTs. (a) Input voltage 0.04 V. (b) Input voltage 0.08 V. Voltage signal solutions $V(x,t)$ (outer) and $W(x,t)$ (inner) are shown for symmetric condensed ionic layer parameters. The black dotted line marks the soliton amplitude peak oscillation.

Figure **7** | Electrical oscillations and rectification obtained in a two-dimensional MT structure, as described

in reference [5]. (Left) Representative tracings of the effect of the input voltage, as indicated, on the MT sheet current oscillations. (Right) Current-to-voltage relationship obtained from integrated, mean currents of individual experiments without any changes in electrochemical gradient.

Figure **8** | Multi-scale electrokinetic model for microtubules. It represents the outer and inner EDLs as coupled transmission lines (green and brown) connected through nanopores in the microtubule wall (yellow), modeling tubulin as a hollow cylindrical structure.

Figure **9** | Ladder transmission lines model. The electric circuit unit cell represents an elementary ring of tubulin dimers shown in Fig. 8.

Figure **10** | MT molecular structure and surface charge distribution. (a) Longitudinal view. (b) Cross-section view. Cryo-electron microscopy data (PDB ID: 3j2u) were used to model the microtubule structure and surface charge distribution. Red indicates negative charges, blue positive charges, and white neutral regions.

Figure **11** | Voltage-dependent nanopore resistance model. a) The pore resistance $R_p(V)$ is calculated for input voltages ranging from 0.01 V to 0.1 V, keeping the other circuit parameters fixed. b) The corresponding current-volrage (I-V) curve shows outward rectification. Red dots represent the calculated data points, and the blue curve corresponds to the fit using the 2S3B energy model.